





Evolution of the magnetic structure in overdoped antiferromagnetic $\text{La}_{1-x}\text{Ca}_x\text{MnO}_3$ ($0.51 \leq x \leq 0.69$) manganites: A neutron diffraction study

M. Pissas ^{1,*}, D. Stamopoulos ², A. Arulraj ³, and K. Prassides ^{4,5}

¹*Institute of Nanoscience and Nanotechnology, NCSR, Demokritos, 15310 Aghia Paraskevi, Athens, Greece*

²*Department of Physics, National and Kapodistrian University of Athens, Zografou Panepistimioupolis 15784, Zografou, Greece*

³*School of Chemical & Biotechnology, SASTA Deemed University, Thirumalaisamudram, Thanjavur - 613 401, Tamilnadu, India*

⁴*Department of Materials Science, Graduate School of Engineering, Osaka Metropolitan University, Osaka 599-8531, Japan*

⁵*Advanced Institute for Materials Research (WPI-AIMR), Tohoku University, Sendai 980-8577, Japan*



(Received 15 September 2022; revised 2 November 2022; accepted 8 December 2022; published 6 January 2023)

The $\text{La}_{1-x}\text{Ca}_x\text{MnO}_3$ series of compounds with antiferromagnetic ground states ($x \geq 1/2$) have been extensively studied due to the novel spin, orbital, and charge-ordering states observed when the calcium concentration is a simple fraction ($x = 1/2, 2/3, \text{ and } 3/4$). The ground states of these compositions have been explained by the Goodenough charge, orbital, and spin ordering model. An important issue remaining is the elucidation of how the ground state changes when x is not a simple number. Here we study the magnetic structure of $\text{La}_{1-x}\text{Ca}_x\text{MnO}_3$ for $0.51 \leq x \leq 0.69$ using powder neutron diffraction measurements supported by magnetization data. For compositions with $0.51 \leq x \leq 0.56$, the magnetic structure, which we term as an incommensurate charge exchange (CE) structure can be described by two propagation vectors $\mathbf{k}_C = [1/2, 0, 1/2]$ and $\mathbf{k}_E = [\varepsilon_E, 0, 1/2]$. In the second one, the component parallel to the \mathbf{a}^* axis of the reciprocal lattice changes with the Mn^{4+} concentration x as $\varepsilon_E \approx x - 1/2$ providing, thus, an unambiguous signature of the adoption of an incommensurate magnetic structure. As x gradually increases, the diffraction data reveal that two magnetic phases—one adopting the incommensurate CE, and one adopting the commensurate “2/3” magnetic structure—co-exist in the concentration regime of $0.57 \leq x \leq 0.61$. Around the simple fraction $x = 2/3$, the magnetic structure can be also described by three propagation vectors, the commensurate $\mathbf{k}_E = [0, 0, 1/2]$, $\mathbf{k}_C = [1/2, 0, 1/2]$, and an incommensurate $\mathbf{k}_{2/3} = [1/3 + \varepsilon_{2/3}, 0, 1/2]$ propagation vector with $\varepsilon_{2/3}$ taking negative/zero/positive values for x smaller than/equal to/larger than $2/3$, respectively. Our experimental results for $0.51 \leq x \leq 0.56$ are neither in favor of a stripe structure consisting of a fine mixture of $x = 1/2$ and $x = 2/3$ phases (phase separation) nor of a defect structure in which an appropriate amount of Mn^{3+} -O sheets have been replaced by Mn^{4+} -O sheets (defect structure). A sinusoidal modulated structure has been used as a possible candidate in explaining the experimental neutron diffraction magnetic Bragg peaks. This result may be linked to the presence of a mixed orbital state of the manganese ions.

DOI: [10.1103/PhysRevB.107.035110](https://doi.org/10.1103/PhysRevB.107.035110)

I. INTRODUCTION

The perovskite manganites, $\text{La}_{1-x}\text{Ca}_x\text{MnO}_3$ ($0 \leq x \leq 1$) play a significant role in understanding strongly correlated electron behavior. Following their initial neutron diffraction study in the 1950s [1], they were also, subsequently, intensively studied because of their connection with the colossal magnetoresistance effect but, most importantly, for their rich physics [2]. Despite the intensive research and progress made so far in understanding this system, the origin of several features is still controversial and not well understood [3].

In particular, in this family of materials, the ratio of $\text{Mn}^{4+}/\text{Mn}^{3+}$ can be changed continuously from 0 to 1 by replacing the trivalent La^{3+} with the divalent Ca^{2+} ion whereas preserving the crystal structure. The mixed valence character of this particular family and the degeneracy of the Mn ion e_g electronic levels lead to a wide variety of phases and phase

transitions as a function of temperature, concentration, pressure, and magnetic field.

A real-space charge- (CO-) and orbital-ordering model is in agreement with the x-ray and neutron diffraction data of compounds with simple fraction concentrations of $x = n/(n+1)$ ($n = 1-4$) of the divalent cation due to the reasonable connection of the observed superstructure Bragg peaks with the $\text{Mn}^{3+}/\text{Mn}^{4+}$ ratio. Specifically, below the charge-ordering temperature (T_{CO}) [4] for $x = 1/2, 2/3, \text{ and } 3/4$, superstructures with periodicities of $2a, 3a, \text{ and } 4a$ have been observed in high-resolution x-ray diffraction patterns [5–8]. The resulting charge- and orbital-ordered structural model is further corroborated below the antiferromagnetic ordering temperature (T_N) by magnetic neutron diffraction studies in which magnetic Bragg peaks with propagation vectors closely related with the simple fraction $x = n/(n+1)$, ($n = 1-4$) are observed [1,5–7,9,10]. An example of the charge, orbital, and spin ordering proposed to explain the diffraction data of the $x = 1/2$ composition is shown in Fig. 1. In this model, below the charge ordering temperature, the additional e_g electrons of

*Corresponding author: m.pissas@inn.demokritos.gr

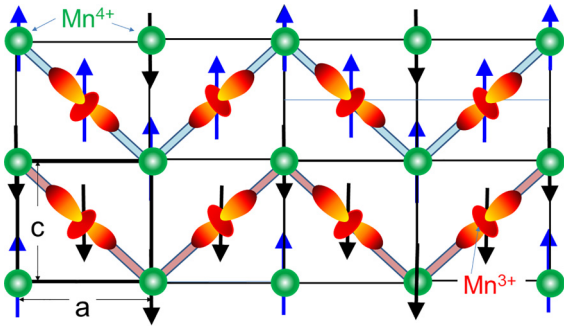


FIG. 1. A layer of the CE structure (Goodenough model) parallel to the ac plane ($Pnma$ setting). In this model, charge, orbital, and spin orders coexist. The structure can be viewed as either ferromagnetic zigzag spin chains coupled antiferromagnetically or, alternatively, Mn^{3+} and Mn^{4+} layers parallel to the ab plane. Spins colored blue and black correspond to the two different sets of ferromagnetic zigzag chains that are antiferromagnetically coupled. The magnetic structure of the Mn^{3+} sublattice can be described by a propagation vector $\mathbf{k}_E = [0, 0, 1/2]$ and that of the Mn^{4+} sublattice by a propagation vector $\mathbf{k}_C = [1/2, 0, 1/2]$.

the Mn atom are arranged in $2D$ sheets, perpendicular to the a axis. In addition, this charge ordering is accompanied by a “zigzag” orbital ordering of the d_{z^2} orbitals. Then, at $T < T_N$, the particular charge and orbital ordering leads to the so-called CE magnetic structure, consisting of zigzag ferromagnetic chains, which are antiferromagnetically coupled along both the b and the c axes [1,3,11,12].

Although the realization of the “integer”-charge-ordered models in interpreting the ground state for $x = n/(n+1)$ ($n = 1-4$) appears conceptually simple and reasonable in order for this model to be generally accepted, we must also understand the ground states when x differs from the simple numbers, $x = 1/2, 2/3$, and $3/4$ as well as the temperature variation of the structural and magnetic modulation vectors. Rodriguez *et al.* [13] combining Rietveld and pair distribution function (PDF) analysis concluded that their results are compatible with neither the strictly ionic model of the $x = 1/2$ compound nor the Mn-Mn dimer model [14]. Instead the PDF data [13] support orbital ordering and partial charge ordering of the two Mn sites. High-pressure neutron diffraction data [15] revealed that the CE-antiferromagnetic state remains stable for the $x = 1/2$ compound, whereas for the $x = 2/3$ composition [16] the “Wigner-crystal” antiferromagnetic state changes to C type with applied pressure. Moreover, it should be noted that the C -type phases observed [17] below the structural and antiferromagnetic transition temperatures for $x = 0.8$ and 0.85 in the $La_{1-x}Ca_xMnO_3$ series display diffuse scattering around the transmission electron microscopy reflections [18] explained via the disordered Jahn-Teller-polaron state [18]. Along the same lines, Loudon *et al.* [19] reported transmission electron microscopy (TEM) data with a convergent beam of 36-\AA diameter but failed to observe scattering from two distinct phases (mixture of phases according to the lever rule) when $x \neq n/(n+1)$, $n = 1-4$ as earlier proposed [20,21]. Interpreting their TEM data, the authors of Ref. [19] claimed that the results are in favor of a uniform periodicity at any doping level between 0.5 and 0.71 , therefore, questioning the

existence of just two types of lattice planes occupied exclusively by Mn^{4+} and Mn^{3+} ions. This general statement is very interesting as it is connected with the idea of the presence of charge-density waves proposed by Khomskii [3] and Milward *et al.* [22], Brey and Littlewood [23], and Cox *et al.* [24] using the phenomenological Ginzburg-Landau theory. Based on the results of nuclear magnetic resonance (NMR) data on the same samples used in the present paper, Koumoulis *et al.* [25] proposed that the NMR line shapes can be reproduced by considering incommensurate modulated phase solitons. Although the available structural data from TEM studies [19–21,26,27] are very informative concerning the concentration variation of the structural modulation in order to have a more detailed insight into the true ground state of the $La_{1-x}Ca_xMnO_3$ compositions for $x \geq 0.5$, the spatial ordering of the magnetic moments especially in the range of $1/2 < x < 2/3$, should be taken into account. We stress that neutron diffraction data for samples with $0.51 \leq x \leq 0.69$ can, therefore, help both to elucidate the controversy, which exists in the relevant literature, and to understand fundamental issues that are related with other strongly correlated electron systems.

For instance, a similar dilemma has been also put forward in the studies of cuprate superconductors [28–32], and of nickelate and cobaltate analogs [32]. Moreover, significant progress has been made recently in the study of insulating antiferromagnetic perovskite manganites regarding the interpretation of the stripe contrast [33–36] observed in scanning transmission electron microscopy data below the charge-ordering temperature [4]. Specifically, Baggari *et al.* [35] used cryogenic scanning TEM measurements and attributed the incommensurate order, observed below and near the charge-ordering temperature of $Bi_{1-x}Sr_{x-y}Ca_yMnO_3$ ($x = 0.65$, $y = 0.47$) to topological defects of the phase field, $\phi(\mathbf{r})$ of the order parameter, $\Delta(\mathbf{r}) = \text{Re}\{\mathbf{A}(\mathbf{r}) \exp[i(\mathbf{q} \cdot \mathbf{r} + \phi(\mathbf{r}))]\}$, where $\mathbf{A}(\mathbf{r})$ and \mathbf{q} are the amplitude and the wave vector, respectively, of the transverse structural modulation. The observed incommensurability with respect to the commensurate, the $q = 1/3$ r.l.u. value was explained by considering that the phase of the order parameter changes randomly. The averaging of this random process produces phase gradients resulting in wave-vector shifts in reciprocal space (an effective incommensurate wave number). On the other hand, Tao *et al.* [33] have explained the charge-ordering transition in $La_{1/3}Ca_{2/3}MnO_3$ using TEM data as a consequence of the proliferation of dislocations of the electronic superstructure and electronic phase separation. They proposed that the incommensurability, studied as a function of temperature, arises from orbital hops ($d_{3x^2-r^2} \rightarrow d_{3y^2-r^2}$) and the accompanying elastic distortions of the four neighboring MnO_6 octahedra.

Here, we present temperature-dependent neutron diffraction and magnetization data on high-quality overdoped $La_{1-x}Ca_xMnO_3$ ($0.51 \leq x \leq 0.69$) polycrystalline samples targeting the detailed study of how the magnetic Bragg peaks evolve with x . The magnetic structure of the samples with $0.5 < x \leq 0.56$ can be described by two sets of magnetic Bragg peaks. The location of the first set can be reproduced by using the propagation vector $\mathbf{k}_C = [1/2, 0, 1/2]$ exactly as for the $x = 1/2$ composition. On the other hand, the second set necessitates indexing using a doping-dependent propagation vector $\mathbf{k}_E \approx [\varepsilon_E, 0, 1/2]$ with

$\varepsilon_E \approx x - 1/2$ smoothly varying with x . A similar incommensurate magnetic-ordering response is also encountered for the two studied $\text{La}_{1-x}\text{Ca}_x\text{MnO}_3$ samples in which the doping levels, $x = 0.63$ and 0.69 straddle the simple fraction value of $2/3$. The magnetic Bragg peaks reproduced using the propagation vectors $\mathbf{k}_E = [0, 0, 1/2]$, $\mathbf{k}_{2/3} = [1/3 + \varepsilon_{2/3}, 0, 1/2]$, and a weak contribution from $\mathbf{k}_C = [1/2, 0, 1/2]$. The incommensurability parameter $\varepsilon_{2/3}$ is zero (slightly negative or positive) for $x = 2/3$ ($x < 2/3$, $x > 2/3$). In the doping regime $0.56 < x < 0.61$, the magnetic Bragg peaks of the experimental neutron diffraction data can be interpreted as a mixture of CE and $x = 2/3$ magnetic phases. As x further increases, the additional Mn^{4+} leads to the predominance of the $x = 2/3$ phase.

II. EXPERIMENTAL DETAILS

$\text{La}_{1-x}\text{Ca}_x\text{MnO}_3$ samples with $x = 0.51, 0.53, 0.545, 0.56, 0.57, 0.58, 0.63,$ and 0.69 were prepared by thoroughly mixing high-purity stoichiometric amounts of CaCO_3 , La_2O_3 , and MnO_2 . The mixed powders were first reacted in air at temperatures up to 1400°C for several days with intermediate grindings. Finally, the samples were slowly cooled to room temperature. Powder neutron diffraction (PND) data were collected with the E6 and E9 diffractometers of the research reactor BER II in Berlin. The PND experiments as a function of temperature in the low-angle range were performed with the E6 diffractometer using a wavelength $\lambda = 2.44 \text{ \AA}$ from the (002) reflection of a pyrolytic graphite monochromator. For crystal structure refinements, data were collected with the E9 diffractometer using wavelengths, $\lambda = 1.798$ and 1.589 \AA [obtained from the (511) and (311) reflections of a vertically focusing Ge monochromator, respectively] with collimation $\alpha_1 = 10'$ (in the pile collimator), $\alpha_2 = 20'$ (the second collimator after the monochromator), and $64 \times 10'$ collimators in front of $64 \text{ }^3\text{He}$ single-detector tubes. The powdered samples were placed in cylindrical vanadium cans ($D = 8 \text{ mm}$) mounted in an Institut Laue-Langevin orange cryostat. DC magnetization measurements were performed with a superconducting quantum interference device magnetometer (Quantum Design). Laboratory x-ray and the neutron powder diffraction patterns were analyzed using the FULLPROF suite of programs [37]. Rietveld refinements of the laboratory x-ray patterns (measured with a D500 Siemens diffractometer) and the neutron diffraction patterns at 300 K showed that all studied samples are single phase materials, crystallizing in the orthorhombic $Pnma$ space group.

III. RESULTS AND DISCUSSION

A. Magnetization data

Magnetization vs temperature data were collected for all $\text{La}_{1-x}\text{Ca}_x\text{MnO}_3$ samples with both zero-field-cooling (ZFC) and field-cooled-cooling (FCC) protocols. In the ZFC mode, the samples were first cooled from 350 to 5 K in the zero magnetic field. Following temperature stabilization, a magnetic field of 100 Oe was applied. Measurements were then performed on warming from 5 to 350 K . In the FCC mode, the data were collected under a magnetic field of 100 Oe on cooling from 350 to 5 K .

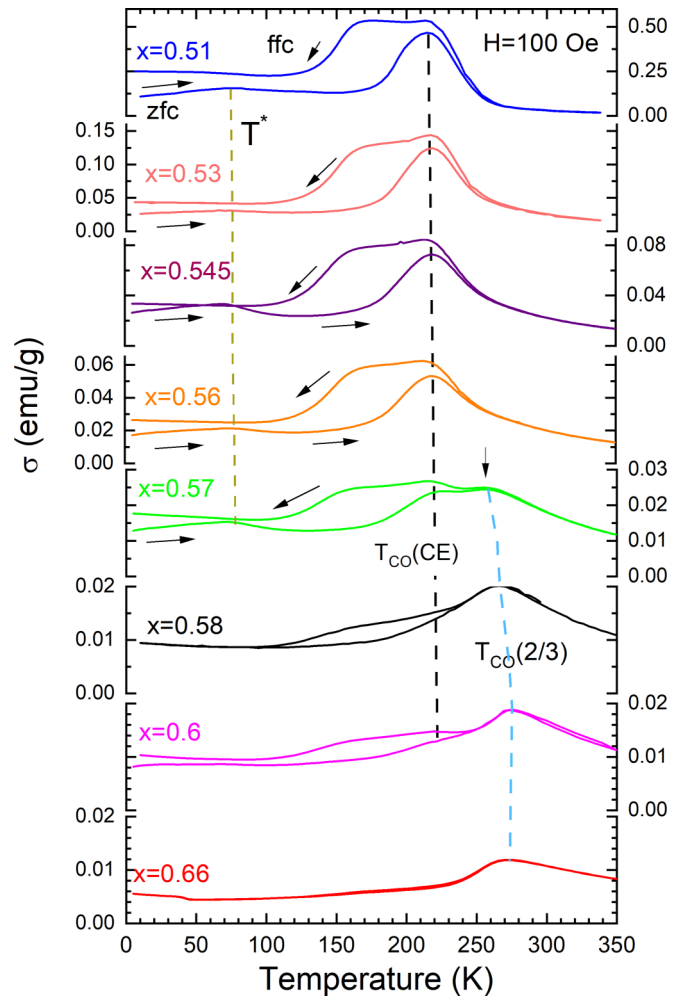


FIG. 2. Temperature variation of the mass magnetic moment for $\text{La}_{1-x}\text{Ca}_x\text{MnO}_3$ samples with $0.51 \leq x \leq 0.66$, measured under ZFC (right arrow) and FCC (left arrow) protocols at an applied field of 100 Oe (see the text for details). T^* represents the temperatures where a broad weak peak is observed, in the ZFC branches for the samples with $0.5 < x \leq 0.57$. $T_{\text{CO}}(\text{CE})$ is defined from the maximum of ZFC magnetization curves for samples with $0.5 \leq x \leq 0.56$. $T_{\text{CO}}(2/3)$ is related with the charge-ordering transition, observed in samples with $x = 2/3$.

Figure 2 shows the temperature variation of the mass magnetic moment σ , measured with the ZFC and FCC protocols. The $\sigma(T)$ curves display pronounced hysteretic behavior between 100 and $\approx 250 \text{ K}$ for all samples. The ZFC branches of the samples with $0.5 < x \leq 0.56$ first display a very broad weak peak around $T^* \approx 75 \text{ K}$ (Fig. 2) and then a peak located at $T_{\text{CO}} \approx 215 \text{ K}$. The corresponding FCC branches show a broad peak, which starts near 215 K and terminates at $\approx 100 \text{ K}$. This hysteretic behavior is indicative of a first-order phase transition corresponding to the so-called CO transition. As the neutron diffraction patterns reveal, long-range antiferromagnetic ordering occurs at a lower temperature, around $T_N \approx 100 \text{ K}$ (*vide infra*).

We stress that the shapes of the magnetization curves are similar to that of the $x = 1/2$ compound [38] for which a transition from a paramagnetic to a ferromagnetic state first occurs at 240 K and, as the temperature decreases, a first-order

ferromagnetic-to-antiferromagnetic transition takes place at 163 K. However, for the $0.51 \leq x \leq 0.56$ samples, there is also a significant difference—the measured magnetic moment in the temperature interval $T_N < T < T_{CO}$ is one to two orders of magnitude smaller than that of the $x = 1/2$ sample [38], most probably reflecting the presence of paramagnetic clusters with ferromagnetic interactions. All $\sigma(T)$ curves for $0.51 \leq x \leq 0.56$ appear similar, implying that for this particular range of compositions, T_{CO} and T_N vary only slightly with x . In this composition interval, the magnetic phase is identified as a modified-CE phase. The magnetization data of the modified-CE phase are in agreement with the results of earlier specific heat measurements [39].

However, as x reaches a value of 0.57, the temperature dependence of the magnetization curves changes drastically. In the range with x between 0.57 and 0.6, the curves now appear as a superposition of those of the $0.51 \leq x \leq 0.56$ samples and of that of the $x = 2/3$ sample (Fig. 2). The latter displays a CO transition at around 280 K. Focusing, for instance, on the $\sigma(T)$ curve of the $x = 0.57$ sample (Fig. 2), we observe a magnetic signal characteristic of the charge-ordering transition of the $x = 2/3$ phase at ≈ 270 K followed by that of the $x = 1/2$ phase at ≈ 250 K. As x increases towards $2/3$, the high-temperature peak moves slightly towards higher temperature, whereas, at the same time, the part of the $\sigma(T)$ curve, corresponding to the modified-CE phase is suppressed and finally disappears when $x > 0.6$. To summarize, there is compelling evidence from the magnetization data of $\text{La}_{1-x}\text{Ca}_x\text{MnO}_3$ that there exists only a single magnetic phase (modified-CE phase) present in the range of $0.5 < x < 0.57$.

In contrast, for $0.57 \leq x \lesssim 0.62$, the magnetic data imply coexistence of two magnetic phases (modified-CE and $x = 2/3$ phases). In this composition range, the magnetic signal is the superposition of those of the two magnetic phases. The T_{CO} values estimated from the present magnetization measurements together with those at higher x from earlier work [10] are shown in Fig. 3. We note that no clear contribution from the minority modified-CE phase was evident in the earlier specific-heat measurements [39].

B. Neutron diffraction data

1. $\text{La}_{1-x}\text{Ca}_x\text{MnO}_3$ compositions with x exceeding 1/2

Although keeping in mind the results of the magnetization measurements, we proceed with the discussion of the neutron diffraction data. Figure 4 shows the temperature evolution of the neutron powder diffraction (NPD) patterns for the $\text{La}_{1-x}\text{Ca}_x\text{MnO}_3$ series of compounds with $x = 0.51, 0.53, 0.545, 0.56, 0.57$, and 0.58 . The data were collected on heating from $T \approx 2$ K. Selected regions of the NPD profiles at 2 K containing the magnetic Bragg peaks are shown in Figs. 5(a)–5(c). In order to allow the novel features of our results to emerge, we also include in Fig. 4 the calculated profiles derived from the standard CE charge-, spin-, and orbital-ordered model [1,5,11] used to describe the crystal and magnetic structures of the $x = 1/2$ composition.

There are several ways to visualize the idealized CE structure. A simple description is that of zigzag ferromagnetic chains coupled antiferromagnetically (Fig. 1). Equivalently, the CE structure can be considered as a layer-type

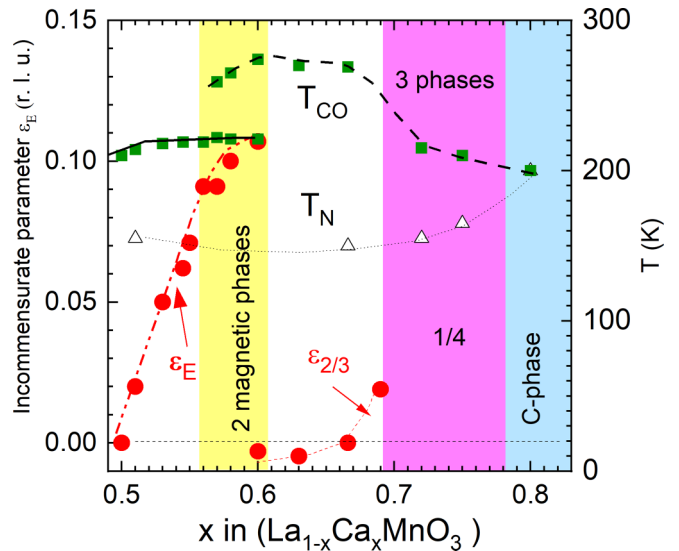


FIG. 3. Variation of T_{CO} , T_N (right axis) and the incommensurate parameters (ϵ_E for $1/2 < x \leq 0.6$ and $\epsilon_{2/3}$ for $0.6 \leq x \leq 0.7$) (left axis) with x for the $\text{La}_{1-x}\text{Ca}_x\text{MnO}_3$ series of compounds. The ϵ_E value for $x = 0.5$, and that for $\epsilon_{2/3}$ are from Refs. [5,6], respectively. The ϵ_E values for the samples with $x = 0.55, 0.6$, and the $\epsilon_{2/3}$ value for the sample with $x = 0.6$ have been obtained by analyzing the powder neutron diffraction data published in Ref. [10]. The data for T_{CO} of the samples $x = 0.72, 0.75$, and 0.8 are from Refs. [7,17].

structure consisting of layers of Mn^{3+} and Mn^{4+} ions stacked in an ABAB... type of arrangement. Long-range magnetic order of the Mn ions leads to the appearance of two distinct families of magnetic Bragg peaks in NPD, each directly associated with one of the two Mn charge states. The magnetic structure can be described by the propagation vectors, $\mathbf{S}_j(\mathbf{R}) = \mathbf{S}_j(\mathbf{R}') \exp[2\pi i \mathbf{k}_j \cdot (\mathbf{R} - \mathbf{R}')]$, with $j = \text{Mn}^{4+}$, Mn^{3+} , and \mathbf{S}_j as the ordered magnetic moment, and \mathbf{R}, \mathbf{R}' as the lattice vectors. The propagation vector associated with the Mn^{4+} -ion sublattice is $\mathbf{k}_C = [1/2, 0, 1/2]$, whereas that for the Mn^{3+} -ion sublattice is $\mathbf{k}_E = [0, 0, 1/2]$. As a result, for the $x = 0.5$ composition (ideal CE structure), two sets of magnetic Bragg peaks are observed—those with Miller indices $(0, 1, 1/2)$, $(1, 1, 1/2)$, $(0, 1, 3/2)$, $(1, 1, 3/2)$, and $(2, 1, 1/2)$, correspond to the E -type Mn^{3+} sublattice, and those with $(1/2, 1, 1/2)$, $[(1/2, 1, 3/2), (3/2, 1, 1/2)]$, $(3/2, 3, 3/2)$, and $(1/2, 3, 1/2)$ correspond to the C -type Mn^{4+} sublattice [17]. The nonzero intensity of the E -type magnetic reflections with $h = \text{integer}$ implies that the magnetic moments of Mn^{3+} ions are ferromagnetically coupled along the a axis. Careful inspection of the diffraction profiles at 2 K for all the samples in the range of $0.51 \leq x \leq 0.58$ (Figs. 4 and 5) reveal that all the expected C -type magnetic Bragg peaks occur precisely at the positions predicted by the $[1/2, 0, 1/2]$ propagation vector. However, notably, a pronounced disagreement is observed between the experimental and the calculated integrated intensities of the unresolved $[(1/2, 1, 3/2), (3/2, 1, 1/2)]$ peak doublet for all compositions in this x range.

Next we consider the second family of magnetic peaks related to the Mn^{3+} -ion sublattice. We find that the $[0, k, (2n + 1)/2]$ peaks are located practically at the positions predicted

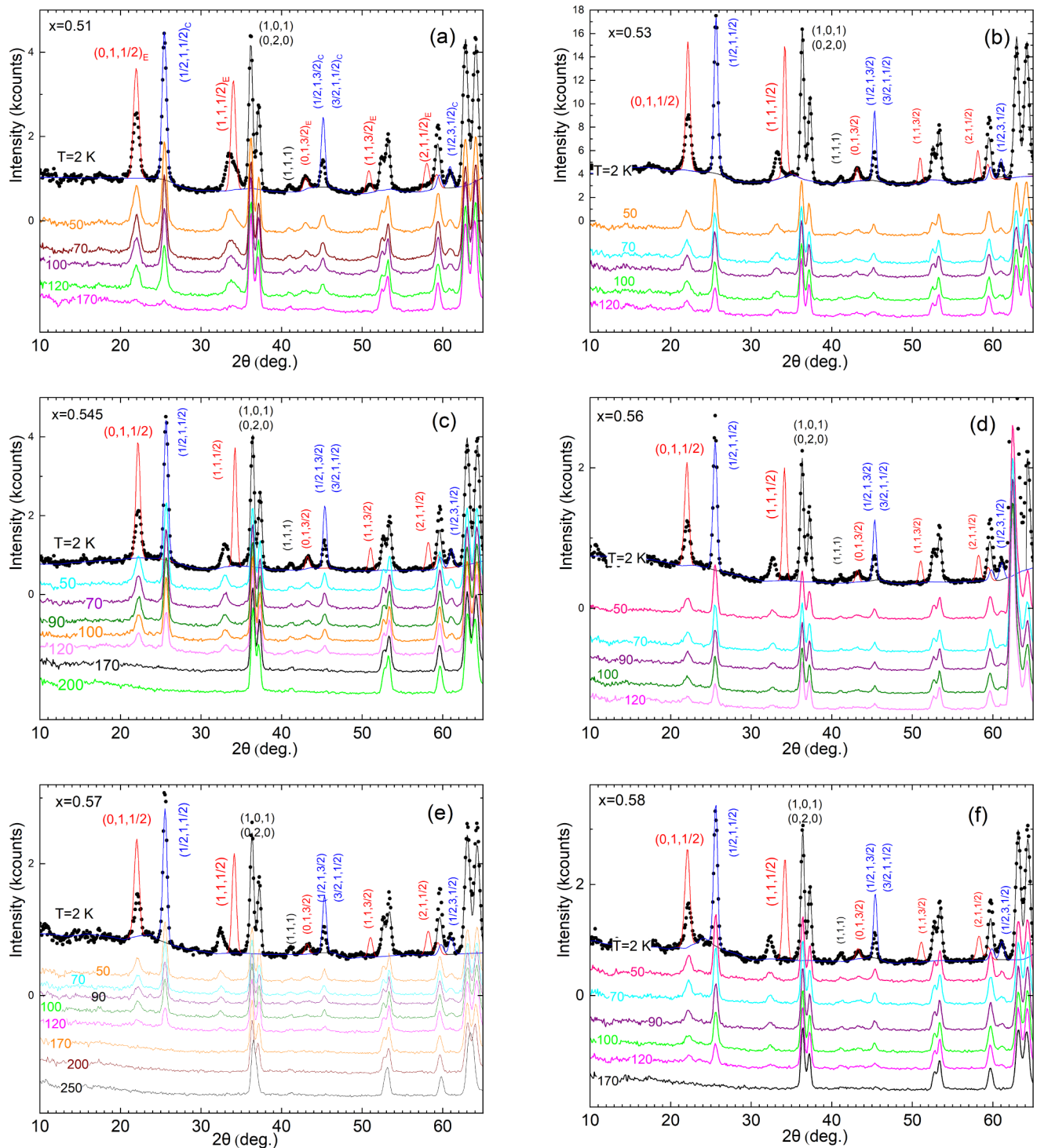


FIG. 4. Powder neutron diffraction patterns ($\lambda = 2.422 \text{ \AA}$) of the $\text{La}_{1-x}\text{Ca}_x\text{MnO}_3$ samples with (a) $x = 0.51$, (b) 0.53 , (c) 0.545 , (d) 0.56 , (e) 0.57 , and (f) 0.58 collected on heating from a base temperature of 2 K . Superimposed on the 2-K experimental patterns, we have included the calculated patterns for the average crystal structure (black line) and for the E - (red line) and C -type (blue line) magnetic structures. The magnetic contributions were calculated using the magnetic structure of the $x = 1/2$ composition, adopted from Ref. [5]. The calculated patterns are included in order to highlight the significant deviations of the current experimental data from the predictions of the ideal $x = 1/2$ CE model.

by the $k_E = [0, 0, 1/2]$ propagation vector. However, a very important observation is that the E -type $(1, 1, 1/2)$ magnetic Bragg peak is located at slightly lower angle in comparison with that calculated theoretically and displays a pronounced broadening. In addition, the higher-order $(1, 1, 3/2)$ and

$(2, 1, 1/2)$ peaks are so broad that their detection is difficult. In contrast, the $(0, 1, 1/2)$ and $(0, 1, 3/2)$ peaks, although broader than the nonmagnetic ones, are narrower than the $(1, 1, 3/2)$ reflection. This selective peak broadening of the E -magnetic structure Bragg peaks has been also observed for

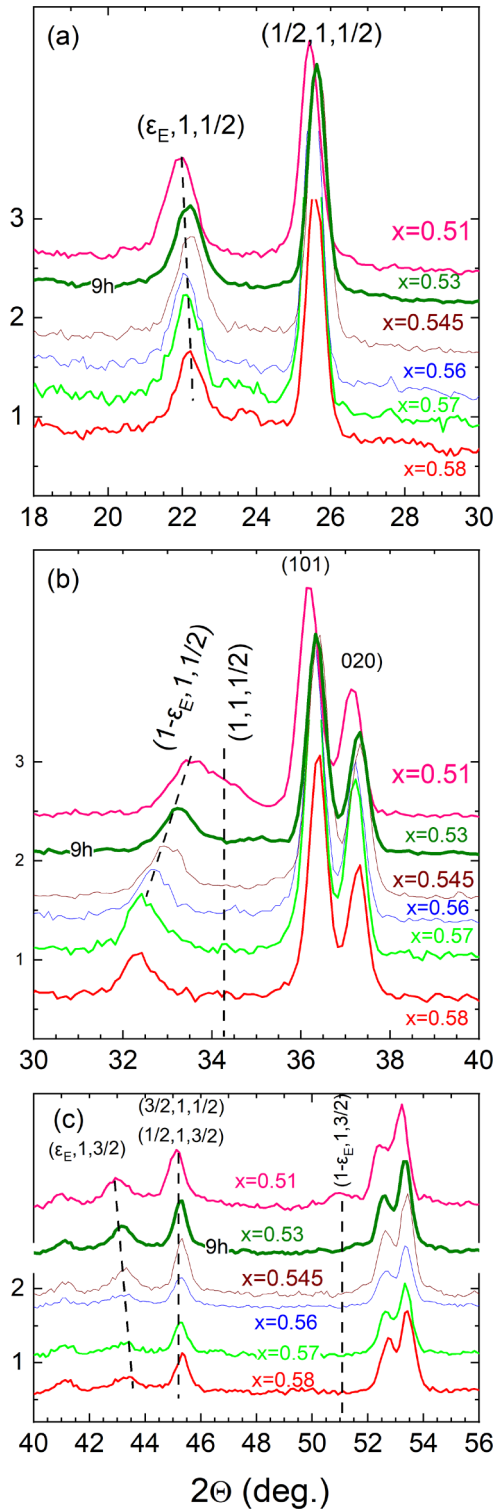


FIG. 5. Composition dependence of the magnetic Bragg peaks of the $\text{La}_{1-x}\text{Ca}_x\text{MnO}_3$ series of compounds measured at $T = 2$ K. Panel (a) shows the first E -type $(\varepsilon_E, 1, 1/2)$ and C -type $(1/2, 1, 1/2)$ magnetic Bragg peaks. The small shift to higher angles with increasing x (dashed line) of the first E -type peak is due to a nonzero value of ε_E . Panel (b) shows the pronounced shift of the E -type $(1 - \varepsilon_E, 1, 1/2)$ Bragg peak with increasing x (dashed line). Panel (c) depicts the shifting to higher angles of the E -type $(\varepsilon_E, 1, 3/2)$ Bragg magnetic peak (dashed line). The C -type magnetic peaks and the nuclear peaks remain practically unshifted.

the nominally $x = 1/2$ sample and has been attributed to the existence of stacking faults [5].

All these experimental findings imply that the simple CE model needs essential modification in order to be applicable for the $\text{La}_{1-x}\text{Ca}_x\text{MnO}_3$ compositions with $x > 0.5$. Indeed we have succeeded to obtain good agreement with the experimental intensity of the C -type magnetic peaks by assuming that both Mn sites participate in the C -type magnetic structure, as we demonstrate in Sec. III C 2. Careful inspection of the evolution of the angular position of the E -type $(1, 1, 1/2)$ magnetic Bragg peak reveals a pronounced shifting towards lower Q values with increasing x away from $x = 1/2$ [see inclined and vertical dashed lines, respectively, in Fig. 5(b)]. In contrast, Fig. 5(c) reveals that as x increases, the higher-order $(0, 1, 3/2)$ E -type peak is displaced towards higher Q values showing the opposite trend. At the same time, the C -type magnetic peaks remain unshifted.

The shifting of the E -type magnetic peaks can be accounted for by including an a -axis component of the \mathbf{k}_E propagation vector that depends on x , namely, $\mathbf{k}_E = [\varepsilon_E(x), 0, 1/2]$. Figure 3 shows the extracted variation of $\varepsilon_E(x)$ with x (red solid circles)—a quasilinear increase with increasing x , $[\varepsilon_E(x) = x - 1/2]$ is observed until a two-phase coexistence regime is reached whence no further significant change is observed. This is an important experimental result implying that the Fourier component with propagation vector $\mathbf{k}_E = (0, 0, 1/2)$ is no longer commensurate with the underlying lattice when $0.5 < x \leq 0.58$.

However, a simple sinusoidally modulated magnetic structure of the Mn^{3+} sublattice with $\mathbf{k}_E = (\varepsilon_E, 0, 1/2)$ is not compatible with the experimental data. For such a magnetic structure, the E -type magnetic peaks, $(h, k, \ell \pm 1/2)$ with $h \neq 0$ should appear with a sizable splitting of the same intensity. Namely, the magnetic Bragg peak $(1, 1, 1/2)$ should split into two peaks of equal intensity, the first $(1 - \varepsilon_E, 1, 1/2)$ located at lower and the second $(1 + \varepsilon_E, 1, 1/2)$ at higher angles in comparison with the $x = 1/2$ case. Similarly, one cannot invoke that antiphase domains are responsible for this peak shifting because magnetic antiphase domains are equivalent to a square modulated structure, which should give rise to split magnetic peaks for $h \neq 0$ (if antiphase domains occur parallel to the a axis). Finally, a CE-type magnetic structure with randomly distributed Mn^{3+} -like stacking faults along the a axis could produce an intensity reduction but fails to reproduce the observed peak shifting.

Besides continuously shifting with increasing x , the E -type magnetic peaks with $h \neq 0$ also exhibit significant broadening, which increases with x , implying short correlation length compared to the crystal and C -type magnetic structure peaks. The overall reduction of the integrated intensity of the E -type peaks with x signifies a diminution of the part of the magnetic moment participating in this type of ordering. On the other hand, in the interval $0.5 < x \leq 0.58$, the C -type magnetic Bragg peaks remain practically unshifted and with the same integrated intensities.

It is clear in all panels of Fig. 4 that the intensity of the magnetic Bragg peaks is reduced as the temperature increases. For the samples with $x = 0.545, 0.57$, and 0.58 for which data are available, the magnetic Bragg peaks disappear for $T \geq 170$ K implying that these compositions are in a para-

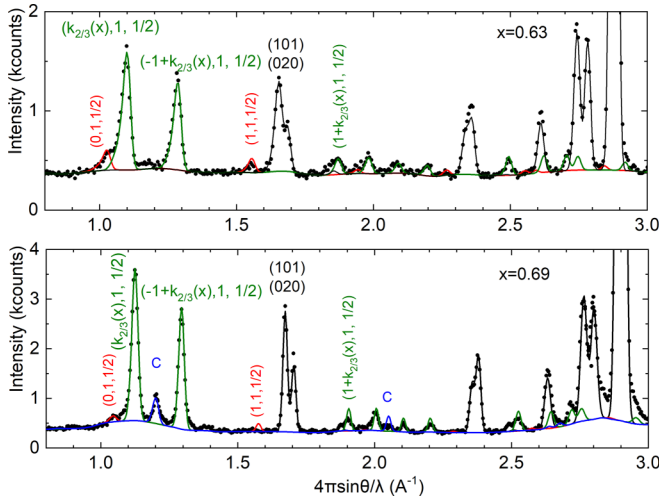


FIG. 6. Powder neutron diffraction patterns of the samples $\text{La}_{1-x}\text{Ca}_x\text{MnO}_3$ with $x = 0.63$ ($\lambda = 1.5798 \text{ \AA}$, upper panel) and $x = 0.69$ ($\lambda = 2.4384 \text{ \AA}$, lower panel) at 2 K. The black lines correspond to the refined average crystal structure patterns. The green lines correspond to the magnetic structures with propagation vectors $\mathbf{k}_{2/3}(x = 0.63) = [0.338(2), 0, 1/2]$, $\mathbf{k}_{2/3}(x = 0.69) = [0.3523(2), 0, 1/2]$, and refined magnetic moments $\mathbf{M} = [2.29(8), 0, 2.38(8)\mu_B]$, and $\mathbf{M} = [2.2(2), 0, 2.2(2)\mu_B]$ for $x = 0.63$ and $x = 0.69$, respectively. The red and blue lines represent the patterns of the magnetic structures with $\mathbf{k}_E = (0, 0, 1/2)$ and $\mathbf{k}_C = (1/2, 0, 1/2)$.

magnetic state for $T > 170 \text{ K}$. It is interesting to note that the position of the magnetic peaks with Miller indices $(1 - \epsilon_E, 1, 1/2)$ does not change with temperature. This means that the parameter ϵ_E is temperature independent within experimental error. The same conclusion also holds for the C-type magnetic peaks.

2. $\text{La}_{1-x}\text{Ca}_x\text{MnO}_3$ compositions with x straddling $2/3$

Interestingly, an additional contribution to the PND profiles appears for the samples with $x = 0.57$ and 0.58 as diffuse scattering now emerges between the magnetic Bragg peaks $(0, 1, 1/2)$ and $(1/2, 1, 1/2)$ [see Figs. 4 and 5(a)]. This grows in intensity as x approaches 0.6 —for this composition, a clear magnetic phase mixture, consisting of modified CE and $x = 2/3$ phases was identified before by PND measurements at $T = 2 \text{ K}$ [10]. These results clearly show that although the TEM [19] and x-ray diffraction studies [40] show a single-phase incommensurate crystal structure, the magnetic structure consists, at least, of two magnetic phases (see the yellow part of the phase diagram depicted in Fig. 3). Essentially, for $x > 0.56$, the sample enters a two magnetic phase regime where two different magnetic structures are needed to account for the experimental neutron diffraction and magnetization data. As x further increases, the additional Mn^{4+} leads to the growth of the $x = 2/3$ phase. Around a calcium concentration of $x = 2/3$, we can reproduce the magnetic Bragg peaks using the propagation vectors $\mathbf{k}_E = [0, 0, 1/2]$, $\mathbf{k}_{2/3} = [1/3 + \epsilon_{2/3}, 0, 1/2]$, and a weak contribution from $\mathbf{k}_C = [1/2, 0, 1/2]$. The incommensurability parameter $\epsilon_{2/3}$ is zero (slightly negative, positive) for $x = 2/3$ ($x < 2/3$, $x > 2/3$) (see Fig. 6).

C. Magnetic models of $\text{La}_{1-x}\text{Ca}_x\text{MnO}_3$ ($1/2 < x \leq 0.58$)

1. Magnetic structure incorporating defect Mn^{4+} sheets

A realistic model based on the CE structure, which can explain some of the observed characteristics of the magnetic Bragg peaks, has been proposed by Ulbrich and Braden [32]. The main idea of this model is that the extra Mn^{4+} atoms occupy sheets parallel to the bc plane and replace the corresponding Mn^{3+} sheets, conserving, however, the ferromagnetic coupling along the zigzag chains [Fig. 7(a)]. Essentially, every Mn^{4+} -defect sheet is followed by a slice of the ideal CE structure, displaced by $c/2$ along the c axis relative to the preceding ideal CE block. The thickness of the blocks with the ideal CE structure can be adjusted in such a way that the nominal stoichiometry of the material is reproduced. In practice, the number of additional defect Mn^{4+} sheets is directly related to the difference in the value of x from the parent $x = 0.5$ composition. At the same time, the average distance separation of the defect sheets regulates the incommensurability.

We have calculated the magnetic scattering amplitude for a crystal consisting of $31a \times 31b \times 31c$ cells using magnetic moments of $\mathbf{S}(\text{Mn}^{3+}) = (1, 0, 2)\mu_B$ and $\mathbf{S}(\text{Mn}^{4+}) = (0, 0, 2.4)\mu_B$ for sites occupied by Mn^{3+} and Mn^{4+} ions, respectively. The result of the calculation is reproduced in Figs. 7(b) and 7(c). Panel (b) [panel (c)] shows the variation of the calculated magnetic intensity $I(q_x, 1, \pm 1/2)$ [$I(q_x, 1, \pm 3/2)$] as a function of the q_x component of the scattering vector. This model reproduces the linear reduction of the wave-number k_E with x . These diffraction peaks are directly related to the dominant experimental observed magnetic peaks $(\epsilon, 1, 1/2)$, $(1/2, 1, 1/2)$, $(1 \pm \epsilon, 1, 1/2)$, $(0, 1, 3/2)$, and $(1/2, 1, 3/2)$. Due to the disorder, the Bragg peaks $(0, \pm 1, \pm 1/2)$ and $(0, \pm 1, \pm 3/2)$ split into pairs $(\pm \epsilon, \pm 1, \pm 1/2)$ and $(\pm \epsilon, \pm 1, \pm 3/2)$, respectively. This agrees with the slight shift of the corresponding experimental magnetic peaks in the powder diffraction patterns. The magnetic peaks with nonzero, q_x values appear as pairs with unequal intensity. The asymmetry depends on the spin direction on the ac plane.

The magnetic powder diffraction pattern calculated from the theoretical scattering cross section is shown in Fig. 7(d). Although this model reproduces adequately the incommensurability of the diffraction peaks $(\pm \epsilon, 1, 1/2)$ and $(1 \pm \epsilon, 1, 1/2)$ and the asymmetry between the $(1 - \epsilon, 1, 1/2)$ and $(1 + \epsilon, 1, 1/2)$ peaks, it produces satellite peaks around the major C-type $(1/2, 1, 1/2)$ magnetic peak in clear disagreement with the experimental data.

2. Sinusoidal modulated magnetic structure

Another possible model which leads to better agreement with the experimental data is based on a sinusoidal modulated magnetic structure. In this model, we consider that the spin density of the Mn sites comprises two components. The first is related to the C-type magnetic Bragg peaks and is given by the equation,

$$\mathbf{C}(\mathbf{n}) = \sum_{\mathbf{n}} (-1)^{n_1+n_2+n_3} [\mathbf{C}_A(0)\delta(\mathbf{x} - \mathbf{R}_{\mathbf{n}}) + \mathbf{C}_B(0)\delta(\mathbf{x} - \tilde{\mathbf{R}}_{\mathbf{n}})],$$

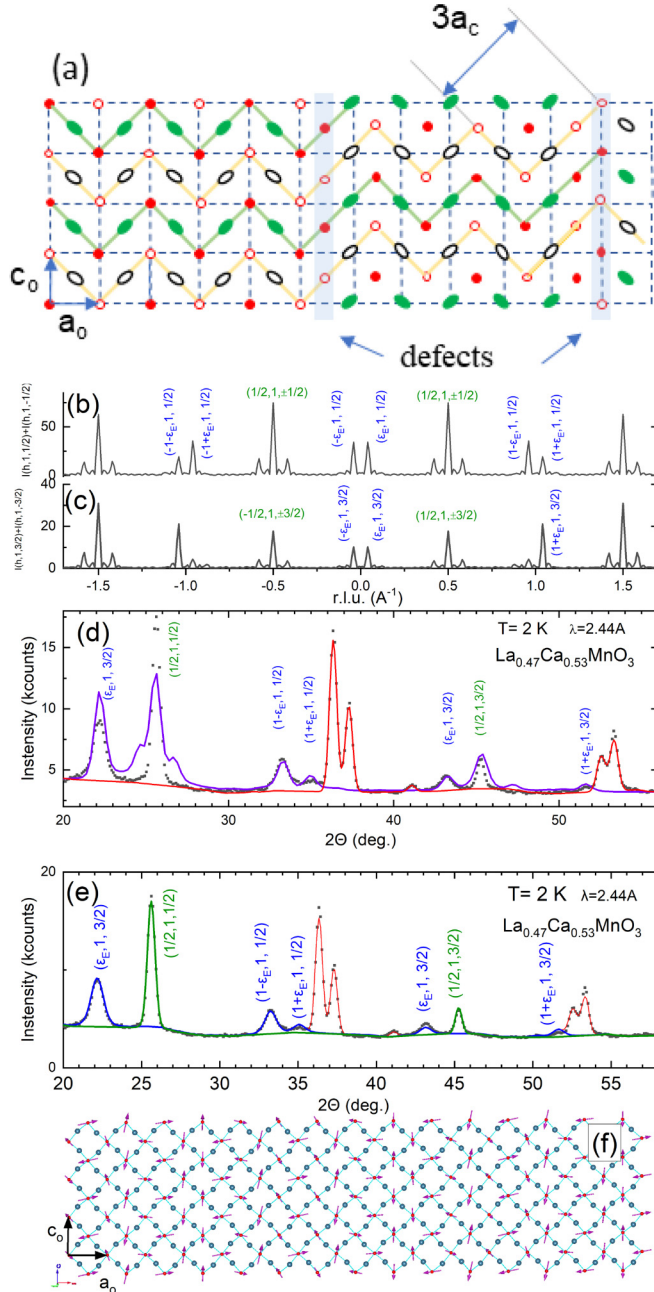


FIG. 7. (a) A possible schematic defect model for the magnetic structure of $\text{La}_{1-x}\text{Ca}_x\text{MnO}_3$ ($1/2 \leq x \leq 0.58$). The extra Mn^{4+} ions randomly replace a Mn^{3+} -ion sheet preserving the ferromagnetic coupling along the zigzag chains. The scattering intensities along the lines $(q_x, 1, \pm 1/2)$ and $(q_x, 1, \pm 3/2)$ calculated from the model of panel (a) are shown in panels (b) and (c), respectively. (d) Comparison of the powder pattern calculated from the scattering intensity of panels (b) and (c) with the experimental neutron diffraction pattern of the sample with $x = 0.53$ (the red continuous line corresponds to the crystal structure, whereas the blue one to the magnetic structure contribution). (e) Rietveld plot of the powder diffraction pattern at $T = 2\text{ K}$ of the sample with $x = 0.53$ based on the sinusoidally modulated magnetic structure [see panel (f) and main text]. (f) View on the $y = 0$ plane of the sinusoidal magnetic structure as refined from the neutron powder diffraction data.

whereas the second one is related to the E -type magnetic Bragg peaks and is given by the equation,

$$\mathbf{E}(\mathbf{n}) = \sum_{\mathbf{n}} (-1)^{n_2+n_3} [\mathbf{E}_A(0) \cos(k_E n_1 a + \phi_1) \delta(\mathbf{x} - \mathbf{R}_n) - \mathbf{E}_B(0) \cos(k_E n_1 a + \phi_2) \delta(\mathbf{x} - \tilde{\mathbf{R}}_n)],$$

where $\delta(\mathbf{x} - \mathbf{R}_n) = \delta(x - n_1 a) \delta(y - n_2 b/2) \delta(x - n_3 c)$ and $\delta(\mathbf{x} - \tilde{\mathbf{R}}_n) = \delta[x - (2n_1 + 1)a/2] \delta(y - n_2 b/2) \delta[x - (2n_3 + 1)c/2]$. The modulation wave-number $k_E = 2\pi\epsilon(x)/a$ is a function of the doping level x .

A representative Rietveld plot of the neutron diffraction data at 2 K for the sample with $x = 0.53$ is shown in Fig. 7(e). The best agreement is achieved for the following spin components, $\mathbf{C}_A(0) = \mathbf{C}_B(0) = (1.1, 0, -1.2)\mu_B$, $\mathbf{E}_A(0) = \mathbf{E}_B(0) = (1.8, 0, 1.8)\mu_B$, $\phi_1 = 0$, $\phi_2 = \pi/2$, and $k_E/(2\pi/a) = 0.053$ (r.l.u.). A schematic of the sinusoidal modulated structure of the $x = 0.53$ compound is shown in Fig. 7(f). A similar analysis can be also applied to the data of the other samples with CE magnetic Bragg peaks. Despite the good agreement with the observed patterns this model should be considered as tentative. A conclusive answer regarding the microscopic origin of the incommensurability of the E -type magnetic Bragg peaks could be obtained by diffraction studies of single crystalline samples when these become available. The incommensurability of the magnetic structures, observed here for nonsimple fractional x values, may be related to a spin modulation which could be associated with the quantum electronic liquid phases and the mixed orbital state $[\cos(\theta/2)d_{3z^2-r^2} - \sin(\theta/2)d_{x^2-y^2}, \sin(\theta/2)d_{3z^2-r^2} + \cos(\theta/2)d_{x^2-y^2}]$, proposed by Tao *et al.* [33]. The orbital mixing angle θ may vary continuously, rotating the e_g orbital around the a axis.

IV. DISCUSSION

Here we refer to some other examples of perovskite manganites displaying incommensurability of the magnetic Bragg peaks and the possible relationship with the present results. For instance, a small incommensurability of the E -type magnetic ordering has been reported in the low-temperature ferroelectric phase of orthorhombic YMnO_3 [41–43]. The small incommensurability was interpreted [42] in terms of either a collinear spin-density wave ordering [43] or the presence of magnetic defects (dephased spins) [42]. In the latter model, the dephased spins create periodically distributed domain walls, which can explain the small incommensurability of the E -magnetic structure. These periodically distributed domain walls are coupled to the ferroelectric domains leading to the creation of multiferroic domains (*via* the exchange striction mechanism) [42]. In our samples, there are no indications of the presence of ferroelectricity, rendering unfavorable a comparable interpretation.

Short-range incommensurate spin correlations (diffuse scattering) [44] were also observed near the E -type (associated with the Mn^{3+} spin network) and C -type (associated with the Mn^{4+} spin network) magnetic Bragg peaks in electron-doped $\text{Pr}_{1-x}\text{Ca}_{1+x}\text{MnO}_4$ with $x < 0.5$. The diffuse scattering

coexists with the CE-type antiferromagnetic order. The incommensurate spin correlations were attributed to domains of Mn^{3+} located parallel to or inclined at 45° with respect to the zigzag ferromagnetic CE chains [44]. However, this model leads to the emergence of additional scattering intensity in neutron diffraction patterns that is not observed in our data.

Incommensurability of the magnetic Bragg peaks associated only with the Mn^{3+} ions has been also observed in single-crystal diffraction experiments of the overdoped double-layered $\text{La}_{1-x}\text{Sr}_{1+x}\text{MnO}_4$ ($x = 0.52$) compound [32,45]. In this system, the incommensurability was explained by using a defect structure in which layers of Mn^{3+} ions are replaced by Mn^{4+} (stripe model) perpendicular to the ferromagnetic zigzag CE chains in such a way that ferromagnetic coupling is not destroyed. As we mentioned above, such a model will lead to additional scattering intensity around the C-type magnetic peaks that is also absent in our diffraction data.

V. CONCLUSIONS

In conclusion, we have arrived at the following results concerning the complex evolution of the magnetic structure of the overdoped $\text{La}_{1-x}\text{Ca}_x\text{MnO}_3$ compositions as the Ca content increases beyond $x = 0.5$ until it reaches and then exceeds the simple fraction of $x = 2/3$. First the simple CE magnetic structure ($\mathbf{k}_C = [1/2, 0, 1/2]$, $\mathbf{k}_E = [0, 0, 1/2]$) established for the $\text{La}_{0.5}\text{Ca}_{0.5}\text{MnO}_3$ phase is no longer valid. For compositions with $0.5 < x \leq 0.56$, we find that the magnetic structure does again consist of two Fourier components—

a commensurate C-type one with $\mathbf{k}_C = [1/2, 0, 1/2]$ and a second incommensurate E-type one with $\mathbf{k}_E = [\varepsilon_E, 0, 1/2]$ with an incommensurate parameter, ε monotonically increasing with increasing x (sinusoidal magnetic structure). As x increases further, the observed magnetic Bragg peaks reveal the existence of a concentration regime, $0.57 \leq x < 0.61$ in which a two-phase magnetic structure is identified. This consists of small domains of the incommensurate CE and the $x = 2/3$ ($\mathbf{k}_{2/3} = [1/3, 0, 1/2]$) magnetic structures. In the next concentration range $0.63 \leq x < 0.7$, the magnetic Bragg peaks correspond to an incommensurate magnetic structure with propagation vectors $\mathbf{k}_E = [0, 0, 1/2]$, $\mathbf{k}_{2/3} = [1/3 + \varepsilon_{2/3}, 0, 1/2]$, and the C-type magnetic structure (which is absent when $x = 2/3$). We have analyzed in detail two models—incorporation of defect Mn^{4+} sheets and a sinusoidal modulated structure—as possible candidates in explaining the observed magnetic Bragg peaks in the neutron diffraction patterns but definitive conclusions should await diffraction studies of single-crystalline materials. The present results should trigger additional theoretical efforts for a more complete understanding of the underlying physics.

ACKNOWLEDGMENTS

We thank the Helmholtz Center, Berlin for access to neutron facilities. This work was financially supported by Grants-in-Aid for Scientific Research JSPS KAKENHI Grants No. JP18K18724, No. JP19H04590, No. JP21H01907, and No. JP22K18693), the Murata Science Foundation, and the Izumi Science and Technology Foundation.

-
- [1] E. O. Wollan and W. C. Koehler, *Phys. Rev.* **100**, 545 (1955).
 - [2] V. Markovich, A. Wisniewski, and H. Szymczak, *Magnetic Properties of Perovskite Manganites and Their Modifications* (Elsevier, Amsterdam, 2014), Chap. 1, pp. 1–201.
 - [3] D. I. Khomskii, *Transition Metal Compounds* (Cambridge University Press, Cambridge, UK, 2014).
 - [4] The terms “charge ordering temperature” or “charge ordering transition” are used here to denote the temperature where the ZFC magnetization curves shows a local maximum, the average crystal structure lattice parameters change abruptly, and satellite Bragg peaks are observed both in TEM and in synchrotron x-ray diffraction measurements. This transition does not necessarily mean ordering of the electric charges.
 - [5] P. G. Radaelli, D. E. Cox, M. Marezio, and S.-W. Cheong, *Phys. Rev. B* **55**, 3015 (1997).
 - [6] P. G. Radaelli, D. E. Cox, L. Capogna, S.-W. Cheong, and M. Marezio, *Phys. Rev. B* **59**, 14440 (1999).
 - [7] M. Pissas, I. Margiolaki, K. Prassides, and E. Suard, *Phys. Rev. B* **72**, 064426 (2005).
 - [8] A. Martinelli, M. Ferretti, and C. Ritter, *J. Solid State Chem.* **239**, 99 (2016).
 - [9] M. T. Fernández-Díaz, J. L. Martínez, J. M. Alonso, and E. Herrero, *Phys. Rev. B* **59**, 1277 (1999).
 - [10] M. Pissas and G. Kallias, *Phys. Rev. B* **68**, 134414 (2003).
 - [11] J. B. Goodenough, *Phys. Rev.* **100**, 564 (1955).
 - [12] J. van den Brink, G. Khaliullin, and D. Khomskii, *Phys. Rev. Lett.* **83**, 5118 (1999).
 - [13] E. E. Rodriguez, T. Proffen, A. Llobet, J. J. Rhyne, and J. F. Mitchell, *Phys. Rev. B* **71**, 104430 (2005).
 - [14] A. Daoud-Aladine, J. Rodríguez-Carvajal, L. Pinsard-Gaudart, M. T. Fernández-Díaz, and A. Revcolevschi, *Phys. Rev. Lett.* **89**, 097205 (2002).
 - [15] D. P. Kozlenko, L. S. Dubrovinsky, I. N. Goncharenko, B. N. Savenko, V. I. Voronin, E. A. Kiselev, and N. V. Proskurnina, *Phys. Rev. B* **75**, 104408 (2007).
 - [16] D. P. Kozlenko, L. S. Dubrovinsky, B. N. Savenko, V. I. Voronin, E. A. Kiselev, and N. V. Proskurnina, *Phys. Rev. B* **77**, 104444 (2008).
 - [17] M. Pissas, G. Kallias, M. Hofmann, and D. M. Többens, *Phys. Rev. B* **65**, 064413 (2002).
 - [18] T. Endo, T. Goto, Y. Inoue, and Y. Koyama, *J. Phys. Soc. Jpn.* **88**, 074708 (2019).
 - [19] J. C. Loudon, S. Cox, A. J. Williams, J. P. Attfield, P. B. Littlewood, P. A. Midgley, and N. D. Mathur, *Phys. Rev. Lett.* **94**, 097202 (2005).
 - [20] S. Mori, C. H. Chen, and S.-W. Cheong, *Nature (London)* **392**, 473 (1998).
 - [21] C. H. Chen and S.-W. Cheong, *Phys. Rev. Lett.* **76**, 4042 (1996).
 - [22] G. C. Milward, M. J. Calderón, and P. B. Littlewood, *Nature (London)* **433**, 607 (2005).
 - [23] L. Brey and P. B. Littlewood, *Phys. Rev. Lett.* **95**, 117205 (2005).
 - [24] S. Cox, J. Singleton, R. D. McDonald, A. Migliori, and P. B. Littlewood, *Nature Mater.* **7**, 25 (2008).

- [25] D. Koumoulis, N. Panopoulos, A. Reyes, M. Fardis, M. Pissas, A. Douvalis, T. Bakas, D. N. Argyriou, and G. Papavassiliou, *Phys. Rev. Lett.* **104**, 077204 (2010).
- [26] R. Wang, J. Gui, Y. Zhu, and A. R. Moodenbaugh, *Phys. Rev. B* **61**, 11946 (2000).
- [27] R. Wang, J. Gui, Y. Zhu, and A. R. Moodenbaugh, *Phys. Rev. B* **63**, 144106 (2001).
- [28] A. Mesaros, K. Fujita, S. D. Ekins, M. H. Hamidian, H. Eisaki, S.-i. Uchida, J. C. S. Davis, M. J. Lawler, and E.-A. Kim, *Proc. Natl. Acad. Sci. USA* **113**, 12661 (2016).
- [29] R. Comin and A. Damascelli, *Annu. Rev. Condens. Matter Phys.* **7**, 369 (2016).
- [30] J. Chang, E. Blackburn, A. Holmes, N. B. Christensen, J. Larsen, J. Mesot, R. Liang, D. A. Bonn, W. N. Hardy, A. Watenphul, M. v. Zimmermann, E. M. Forgan, and S. M. Hayden, *Nat. Phys.* **8**, 871 (2012).
- [31] I. Vinograd, R. Zhou, M. Hirata, T. Wu, H. Mayaffre, S. Krämer, R. Liang, W. Hardy, D. Bonn, and M.-H. Julien, *Nat. Commun.* **12**, 3274 (2021).
- [32] H. Ulbrich and M. Braden, *Physica C* **481**, 31 (2012), (and references therein).
- [33] J. Tao, K. Sun, W.-G. Yin, L. W. H. Xin, J. G. Wen, W. Luo, S. J. Pennycook, J. M. Tranquada, and Y. Zhu, *Sci. Rep.* **6**, 37624 (2016).
- [34] J. Tao, K. Sun, J. M. Tranquada, and Y. Zhu, *Phys. Rev. B* **95**, 235113 (2017).
- [35] I. El Baggari, B. H. Savitzky, A. S. Admasu, J. Kim, S.-W. Cheong, R. Hovden, and L. F. Kourkoutis, *Proc. Natl. Acad. Sci. USA* **115**, 1445 (2018).
- [36] B. H. Savitzky, I. El Baggari, A. S. Admasu, J. Kim, S.-W. Cheong, R. Hovden, and L. F. Kourkoutis, *Nat. Commun.* **8**, 1883 (2017).
- [37] J. Rodríguez-Carvajal, *Physica B* **192**, 55 (1993).
- [38] M. V. Abrashev, J. Bäckström, L. Börjesson, M. Pissas, N. Kolev, and M. N. Iliev, *Phys. Rev. B* **64**, 144429 (2001).
- [39] M. Pissas and D. Koumoulis, *J. Appl. Phys.* **122**, 143902 (2017).
- [40] M. Pissas, D. Stamopoulos, and K. Prassides (2022) (unpublished).
- [41] S. Quezel, J. Rossat-Mignod, and E. Bertaut, *Solid State Commun.* **14**, 941 (1974).
- [42] N. Terada, T. Nakano, C. V. Colin, A. Stunault, N. Qureshi, B. Ouladdiaf, and H. Sato, *Phys. Rev. B* **105**, 144403 (2022).
- [43] A. Muñoz, J. A. Alonso, M. T. Casais, M. J. Martínez-Lope, J. L. Martínez, and M. T. Fernández-Díaz, *J. Phys.: Condens. Matter* **14**, 3285 (2002).
- [44] F. Ye, S. Chi, J. A. Fernandez-Baca, A. Moreo, E. Dagotto, J. W. Lynn, R. Mathieu, Y. Kaneko, Y. Tokura, and P. Dai, *Phys. Rev. Lett.* **103**, 167202 (2009).
- [45] H. Ulbrich, D. Senff, P. Steffens, O. J. Schumann, Y. Sidis, P. Reutler, A. Revcolevschi, and M. Braden, *Phys. Rev. Lett.* **106**, 157201 (2011).